Chinese Chemical Letters 36 (2025) 110087

Contents lists available at ScienceDirect

Chinese Chemical Letters

journal homepage: www.elsevier.com/locate/cclet

High-efficiency Fe(III)-doped ultrathin VO_2 nanobelts boosted peroxydisulfate activation for actual antibiotics photodegradation

Shukun Le[a], Peng Wang[a], Yuhao Liu[b], Mutao Xu[b], Quansheng Liu[a], Qijie Jin[b], Jie Miao[b], Chengzhang Zhu[b,c,*], Haitao Xu[b,*]

[a] *Inner Mongolia Key Laboratory of High-Value Functional Utilization of Low Rank Carbon Resources, Chemical Engineering College, Inner Mongolia University of Technology, Hohhot 010050, China*

[b] *School of Environmental Science and Engineering, Nanjing Tech University, Nanjing 210009, China*

[c] *Key Laboratory of Optic-electric Sensing and Analytical Chemistry for Life Science, MOE, Qingdao University of Science and Technology, Qingdao 266042, China*

ARTICLE INFO

Article history:
Received 30 January 2024
Revised 19 April 2024
Accepted 4 June 2024
Available online 4 June 2024

Keywords:
Fe-doped VO_2 nanobelts
Photodegradation
Persulfate activation
Antibiotics removal
Bimetallic cycle

ABSTRACT

It has been challenging for Fe(III) regeneration in Fe-based photocatalysts for continuous peroxydisulfate (PDS) activation due to the lower ability to reduce Fe(III). In this work, Fe-doped ultrathin VO_2 (Fe-VO_2) nanobelts were synthesized for purifying metronidazole (MNZ) *via* PDS activation. As an efficient Fenton-like catalyst for PDS activation, 2 wt% Fe-doped VO_2 can remove 98% of MNZ within 40 min and exhibits impressive recyclability. The synergistic effect of Fe-VO_2 and Fe(III) activated PDS boosted the photocatalytic performance. Moreover, $SO_4^{\bullet-}$, h^+, $O_2^{\bullet-}$, $^1O_2$, and $^{\bullet}OH$ were the main reactive radicals. The effects of initial MNZ concentration, Fe-VO_2, PDS dosage, and various anions/cations on MNZ removal by the Fe-VO_2/PDS/Vis system were studied. The intermediates of MNZ degradation and possible pathways were determined by density function theory (DFT) calculations and HPLC-MS. This study provided a sustainable technology using Fe-doped ultrathin VO_2 nanobelts for photocatalytic PDS activation and decontamination of pharmaceutical wastewater.

Antibiotics were generously applied for controlling infectious diseases and ignored their toxicity, which leading to the misuse of antibiotics and resulting in antibiotic accumulation and an abundance of multi-resistant bacteria in the water environment [1-3]. The freshwater was contaminated not only by human medicine but also by practically available antibiotics used by veterinarians. The variety of antibiotic contaminants and their concentration in the aquatic environment were steadily increasing, due to human and animal excretion with forms of antibiotic invariance and activity [4-6]. Metronidazole (MNZ) has been widely used as an antibiotic for the treatment or prevention of systemic or local infections caused by anaerobic bacteria [7,8]. However, MNZ has potential carcinogenicity, mutagenicity, and genotoxicity, it is difficult to degrade naturally in water environment owing to its characteristics of stable structure and strong antibacterial ability. Moreover, the extensive release of MNZ into the environment has led to the accumulation of toxicity in aquatic organisms and will have adverse effects on humans and ecology [9-11]. Thus, various physical and chemical processes and biological approaches have already been applied to remove antibiotics from wastewater, and there was a strong and growing desire to find more sustainable and efficient antibiotic removal methods.

Advanced oxidation process (AOPs) has received considerable interest as one of the most popular green methods for the complete degradation of macromolecular contaminants in water by producing free radicals and destroying them into small molecules with low or no toxicity [12-14]. Activating hydrogen peroxide (H_2O_2) *via* homogeneous and heterogeneous Fenton processes to produce $^{\bullet}OH$ radicals has been considered as one of the commonly available AOPs, providing an advantageous strategy for removing various hard-to-degrade pollutants [15-17]. However, the comparatively lower efficiency, limited acidic pH requirements, instability and the safety management of H_2O_2 are the drawbacks preventing their development. Consequently, the exploration of reliable oxidant alternatives to H_2O_2 was essential to realize cost-efficient water purification technologies. Persulfate (PS), including peroxymonosulfate (PMS) and peroxydisulfate (PDS), is considered to be an ideal alternative oxidant that can be rapidly activated by various methods to produce sulfate radicals ($SO_4^{\bullet-}$) [18-22]. AOPs based

---

* Corresponding authors at: School of Environmental Science and Engineering, Nanjing Tech University, Nanjing 210009, China.

E-mail addresses: zhucz@njtech.edu.cn (C. Zhu), htxu@njtech.edu.cn (H. Xu).

https://doi.org/10.1016/j.cclet.2024.110087

on $SO_4^{\bullet -}$ are increasingly used, and $SO_4^{\bullet -}$ has a higher redox capacity (2.5–3.1 V) than $^{\bullet}OH$ (1.8–2.7 V) [23,24]. Solid PDS is easier and safer to use, transport and store than liquid H_2O_2. However, PDS has been found to be slow to react to target contaminants at ambient temperatures. Transition metal oxides have been used as activators for the activation of PDS due to their strong activation capability and reduced energy consumption [25-27]. Photocatalysis as an AOPs technology is considered to be an opportune approach for wastewater treatment. It is worth noting that PDS can also be reactivated with photogenerated electrons produced by the photocatalyst. Accordingly, the development of Fenton-like photocatalysts for PDS activation to remove antibiotics under solar light is of great importance.

Vanadium dioxide (VO_2) provides a unique 2D layered structure and is an excellent transition metal oxide material [28]. Various applications of VO_2 have been extensively investigated due to its special physical and chemical properties, such as catalysts, lithium-ion cells, solar cells, gas sensors, optoelectronic components, electrochromic devices and electro-optical switches [29-32]. In addition, VO_2 had a unique narrow band gap of 0.7 eV and are favorable candidates for light conversion applications [33]. The N-type narrow band gap semiconductor material VO_2 is widely used in the field of photocatalysis due to its diversified crystal forms, which can be transformed into each other at a certain temperature, the growth direction can be controlled by elemental doping, and the excellent light absorption performance [34]. In addition, recent studies have shown that ultrathin two-dimensional nanosheets with larger specific surface area, improved permeability and higher porosity have more obvious advantages in the process of $^1O_2$ generation [35,36]. In comparison with other structures, nanosheets provide a shorter distance for the transfer of photogenerated charges, thus accelerating the charge transfer and the electron-hole separation [37-40]. Specifically, the high redox capacity allows VO_2 to be well adapted to PDS activation. However, the photocatalytic activity of VO_2 remains relatively low and has been modified by various methods to improve the photocatalytic performance of the system. Elemental doping of semiconductors has been found to be a valuable and effective approach to tune physicochemical properties such as structure, physical properties, composition and photocatalytic properties in various modification methods, leading to their increased suitability in the field of photocatalysis [41-43]. Furthermore, exploiting the interaction between semiconductor materials and Fe^{3+} is considered to be one of the effective methods to overcome the slow Fe^{3+}/Fe^{2+} cycle kinetics of the Fenton reaction [44-46], Driven by visible light, the e^- provided by V^{4+} is accepted by Fe^{3+} to generate Fe^{2+}, which activates PDS, thereby promoting the Fenton-like reaction cycle [47-49]. The loss of e^- converts V^{4+} to V^{5+}, providing the possibility of metal self-circulation [50,51] and also providing sufficient active sites for the oxidation of antibiotics. In this case, the design of 2D ultrathin Fe-doped VO_2 nanobelts structures as photocatalysts for PDS activation under solar illumination for antibiotic removal is intriguing but challenging.

Hence, a $SO_4^{\bullet -}$-based Fenton-like photocatalysts 2D ultrathin Fe-doped VO_2 (Fe-VO_2) nanobelts were synthesized in this work by hydrothermal-calcination process. The synthesized Fe-VO_2 photocatalysts were thoroughly characterized in terms of their components and structures using various characterization methods. Meanwhile, the influence of different conditions on the performance of photocatalytic MNZ removal in the presence of PDS under solar light illumination, such as the amount of Fe-VO_2, the PDS concentrations, and the MNZ content, was also discussed. To demonstrate the photodegradation performance of Fe-VO_2 nanobelts on PDS activation in a real environment, reusability experiments and typical anions and cations (K^+, Ca^{2+}, NO_3^-, HPO_4^{2-}, SO_4^{2-}, and Cl^-), various antibiotics, different pH values and real water experiments were performed. Through the density function theory (DFT) analysis and various advanced experimental techniques, the feasible degradation pathways of MNZ were comprehensively investigated, and a plausible mechanism of Fe-VO_2 photocatalyst for MNZ removal *via* PDS activation was established.

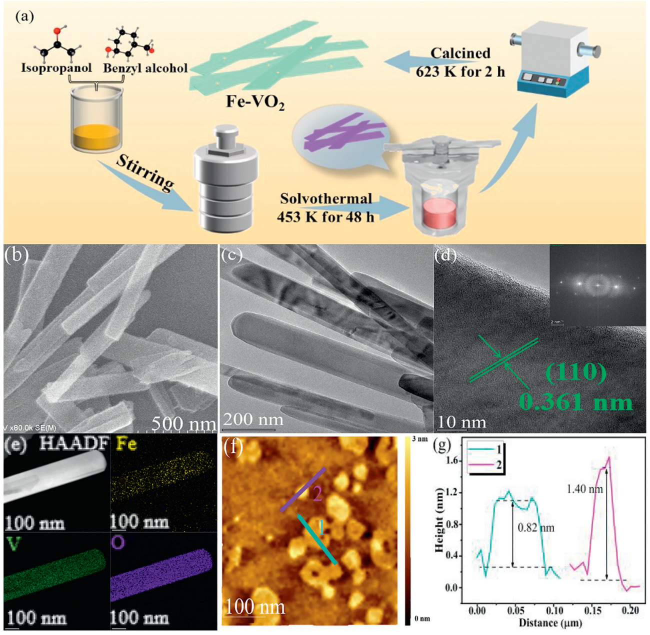

Fig. 1. The results of Fe-VO_2: (a) The hydrothermal synthesis process, (b) SEM image, (c) TEM image, (d) HRTEM image. Inset: the corresponding SAED pattern. (e) Mapping shows the different element with different color Fe (yellow), V (green), and O (purple). (f) AFM image and (g) height profile of the Fe-VO_2.

Details of the chemicals and materials, activity assessment, characterization and DFT calculation were presented in Text S1 (Supporting information).

First, 1.82 g of V_2O_5 powder was added to a mixture of isopropanol (32 mL) and benzyl alcohol (4 mL), and heated to 328 K for 20 min to obtained the light-yellow oligomer. Then, the above oligomer was dispersed in deionized water, and $FeCl_3 \cdot 6H_2O$ was added and stirred vigorously for 10 min. The resultant mixture was transferred to a Teflon-lined autoclave and heated at 453 K for 48 h. After cooling to room temperature, the powders were separated by centrifugation, washed with deionized water and ethanol, and dried in an oven at 353 K for 30 min. Subsequently, the ground above powder was placed in a tube furnace and calcined at a heating rate of 276 K/min to 623 K for 2 h. After cooled naturally to room temperature, and ground to obtain a black powder of Fe-VO_2. The samples prepared with varying the addition amount of $FeCl_3 \cdot 6H_2O$ (1 wt%, 2 wt%, 3 wt%), and denoted as 1-Fe-VO_2, 2-Fe-VO_2, 3-Fe-VO_2, respectively. Meanwhile, the Fe contents were determined by ICP measurements, and the results were shown in Table S1 (Supporting information). Pure VO_2 was fabricated by a similar method without the addition of $FeCl_3 \cdot 6H_2O$. The whole fabrication route was shown in Fig. 1a.

The scanning electron microscopy (SEM) and transmission electron microscopy (TEM) images of the Fe-VO_2 nanobelts were shown in Figs. 1b and c The uniformly smooth Fe-VO_2 nanobelts with lengths of a few μm, widths of 50–100 nm, and thicknesses of 1–2 nm were synthesized. The high-resolution transmission electron microscopy (HRTEM) image of labelled region shown a d-spacing of 0.361 nm, which is attributed to the (110) face of VO_2 [52]. The results were consistent with the corresponding selected area electron diffraction (SAED) image (inset of Fig. 1d), which has distinct diffraction spots, demonstrating its single-crystal character. The energy dispersive spectrometer (EDS) mapping showed a

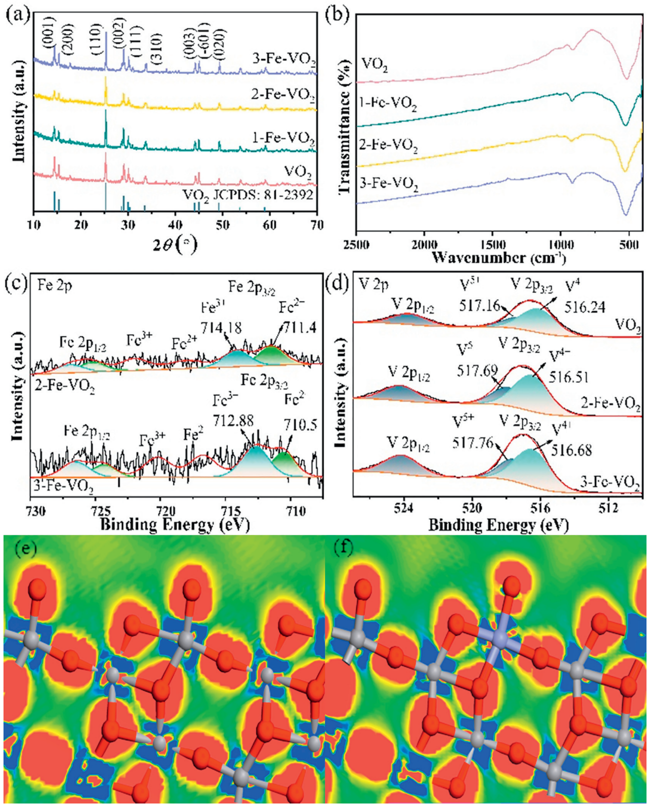

Fig. 2. (a) XRD patterns and (b) FTIR spectra of the as-prepared samples, XPS spectra of (c) Fe 2p and (d) V 2p. Differential charge densities of the (e) VO_2 and (f) Fe-VO_2 using DFT calculations. The red and blue isosurfaces correspond to the increase in the number of electrons and the depletion zone, respectively. Red represents O, gray represents V, and purple represents Fe.

uniform distribution of Fe and V elements (Fig. 1e). The height of the samples was characterized by atomic force microscopy (AFM). As shown in Figs. 1f and g, the thickness of the Fe-VO_2 nanobelts were 0.82 nm and 1.40 nm, respectively.

The X-Ray diffraction (XRD) patterns using different contents of Fe-doped VO_2 were shown separately in Fig. 2a. Clearly, all the diffraction peaks in Fe-VO_2 matched well with the standard diffraction pattern of VO_2 (JCPDS No. 81–2392) [53]. Meanwhile, the XRD pattern did not change significantly after Fe doping, and no characteristic peaks of Fe or iron oxide were found, which was presumably due to the low Fe content in the composites. FTIR spectra were used to determine the structural information, and the FTIR spectra of the prepared samples are shown in Fig 2b. There are spectral bands associated with V-O stretching vibrations between 450 and 1150 cm^{-1} for VO_2 and different contents of Fe-doped VO_2 samples. The band located at about 923 cm^{-1} is attributed to V=O and V-O-V stretching vibrations. In addition, the band appearing at 530 cm^{-1} could be considered as in-plane and out-of-plane V-O-V bending vibrations [54].

The valence state and electronic structure of the Fe-VO_2 nanobelts were confirmed by X-ray photoelectron spectroscopy (XPS) and DFT calculations. The chemical valence states of the samples were examined by XPS. Compared with pure VO_2, the XPS spectra of Fe-VO_2 contained V, Fe and O (Fig. S1a in Supporting information). As shown in Fig. S1b (Supporting information), the O 1s spectrum of pure VO_2 and Fe-VO_2 existed three peaks centered at 529.76, 531.09 and 533.00 eV. The binding energy of 529.76 eV was attributed to O^{2-} in the VO_2 lattice. The binding energy of 531.09 eV was suggested to be the presence of an oxygen absorption peak on the surface of VO_2, indicating the adsorption of free hydroxyl groups or H_2O [55]. The peak at 533.00 eV was ascribed to the oxygen vacancies created in the VO_2 nanobelts, which were shifted with the addition of Fe^{3+} by 1.91 and 1.68 eV, respectively, assumably resulting from the formation of Fe-O bonds. As shown in Fig. 2c, the Fe^{2+} and Fe^{3+} peaks of Fe-VO_2 were located at 711.4 and 714.28 eV, ascribed to the stronger oxidizing potential of Fe^{3+} that will oxidize V^{4+} during the hydrothermal reaction, leading to the appearance of Fe^{2+}. Meanwhile, the corresponding satellite peaks of Fe^{3+} and Fe^{2+} appeared at 718.18 and 725.58 eV, respectively [56]. The increase of Fe^{3+} leads to the increase of Fe^{2+} conversion during the hydrothermal reaction. In V 2p spectrum (Fig. 2d), V $2p_{3/2}$ and V $2p_{1/2}$ appeared at binding energies of 516.58 and 523.68 eV, respectively, where 516.24 eV corresponded to V(IV) in VO_2 and the peak at 517.16 eV to V(V) [57]. With the continuous addition of Fe ions, V(IV) and V(V) are positively shifted by 0.17 and 0.07 eV, respectively, which can be attributed to the interaction between metals during the hydrothermal process. Some strong oxidizing Fe(III) oxidizes V(IV) to V(V) [58-60].

The charge density distribution between the dispersed Fe and VO_2 nanobelts was further investigated by DFT calculations. As shown in Fig. 2e, the red isosurfaces around the V atoms indicated that the electrons were released from the V atom and transferred to the nearby O atom. As for Fe-VO_2 (Fig. 2f), the doped Fe atoms had mushroom-like charge density distributions. The Fe atoms dispersed in the VO_2 nanobelts carry positive charges, which was consistent with the XPS results in Fig. 2c. Supported by the VO_2 nanobelts, the electron delocalizes on the Fe atoms and moves toward the neighboring O atoms. The red isosurfaces around the Fe atoms (Fig. 2f) indicate the asymmetrically distributed residual partial charge densities on the isolated Fe atoms.

The optical properties of as-fabricated photocatalysts were presented in Text S2 (Supporting information).

The photocatalytic degradation performance of the as-constructed Fe-VO_2 materials for MNZ was investigated. Fig. 3a demonstrated that individual light, persulfate, or photocatalyst are not effective for the removal of MNZ, whereas when all three were used in combination, the removal rate of MNZ was significantly increased. The 2-Fe-VO_2/PDS/visible light system exhibited the best photodegradation efficiency of MNZ, where almost 98% degradation was achieved within 40 min, outperforming other photocatalysts in the recent reports (Table S2 in Supporting information). Excitation of VO_2 under light generated photogenerated e^-, which promoted the conversion of neighboring Fe^{3+} to Fe^{2+}. Subsequently, Fe^{2+} participated in PDS activation to generate $SO_4^{\bullet-}$ [61], which reduced the recombination rate of the photogenerated e^--h^+ pairs, demonstrating the synergistic effect of photocatalytic technology and PDS activation. The excess Fe^{3+} would react with PDS to form $S_2O_8^{\bullet-}$, which had lower oxidizing ability than $SO_4^{\bullet-}$, leading to a reduction in photodegradation efficiency [62]. The mineralization efficiency of MNZ in the 2-Fe-VO_2/PDS/Vis system was 81% in the TOC test (Fig. S3 in Supporting information). In summary, the 2-Fe-VO_2/PDS/Vis system presented higher photocatalytic activity and mineralization ability compared to other systems.

The effect of various environmental factors on the photocatalytic activity of the Fe-VO_2/PDS/Vis system was investigated. Since it was necessary to consider cost control in practical applications, the effects of adding different doses of PDS and photocatalyst to the Fe-VO_2/PDS/Vis system on MNZ degradation were investigated. The dosage of PDS in the range of 0.2–0.5 g/L enhanced the photodegradation rate with increasing PDS concentration (Fig. 3b). However, the excessive amount of PDS caused $SO_4^{\bullet-}$ to react with $S_2O_8^{2-}$ to form $S_2O_8^{\bullet-}$, resulting in the decrease in the degradation rate. The oxidative capacity of the system increased continuously when the addition amount was increased from 0.2 g/L to 0.5 g/L (Fig. 3c), which could be attributed to the increase in the activa-

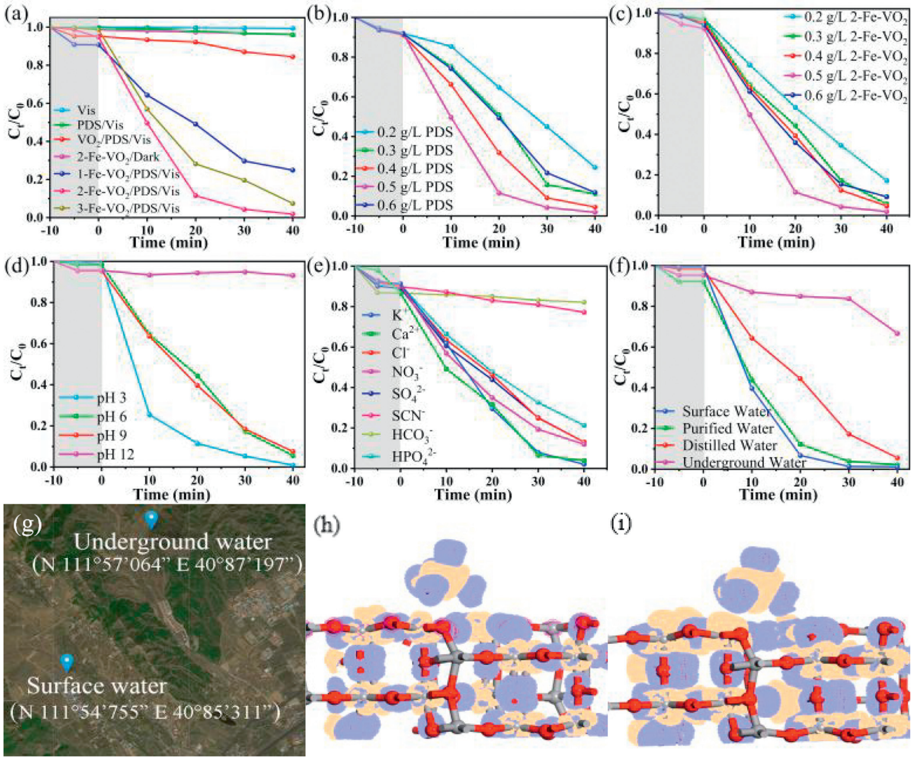

Fig. 3. (a) Control experiments with different Fe-VO_2 on MNZ degradation. (b) Effects of PDS dosage, (c) effects of catalyst dosage, (d) effects of pH on MNZ removal over Fe-VO_2. (e) Effects of coexisting cation and anions on MNZ removal over Fe-VO_2 photocatalyst. (f) Degradation of MNZ in simulated natural water by Fe-VO_2. (g) The specific location longitude and latitude of the natural water, Charge density difference induces by PDS on VO_2 (h) and Fe-VO_2 (i). Electron excess and deficiency are represented as yellow and purple isosurfaces, respectively. [MNZ] = 20 mg/L, [PDS] = 0.5 g/L, [Catalyst] = 0.5 g/L, pH 6. Only one element was changed in the respective experiment, while the other parameters were held constant in accordance with the previous description.

tion sites of the reaction due to the increased addition of photocatalyst. However, when the photocatalyst dosage was increased to 0.6 g/L, the degradation rate decreased significantly, due to the excess Fe^{3+} reacting with PDS to form $S_2O_8^{\bullet-}$. Finally, the optimal PDS dosage and photocatalyst loading were 0.5 g/L and 0.5 g/L to obtain fast radical generation and high degradation efficiency.

The initial concentration of pollutants in water is an important indicator of water quality, and the effect of MNZ concentration on the Fe-VO_2/PDS/Vis system was investigated. The higher the concentration of MNZ, the lower the degradation efficiency of MNZ by the Fe-VO_2/PDS/Vis system (Fig. S4 in Supporting information). The degradation rate of MNZ remained above 96% at initial concentrations of 10 mg/L and 20 mg/L, while the degradation efficiency of MNZ decreased slowly with increasing MNZ concentrations from 20 mg/L to 50 mg/L. The degradation rate in the Fe-VO_2/PDS/Vis system was limited by the reactive radicals with high concentrations of MNZ.

The effect of initial pH on the degradation process of MNZ was explored as shown in Fig. 3d. According to the p*K*a value of MNZ ($pK_a = 2.58$), the molecule was almost in the protonated form at pH $\leq$ 2 and amphipathic at pH $\geq$ 4. The PDS activation was facilitated by the prolonged presence of Fe^{2+} in solution under acidic conditions. Therefore, the system exhibited excellent degradation efficiency in the pH range of 3–9 with MNZ in amphipathic ionic form with positive surface charge, promoting electrostatic interactions between MNZ and $SO_4^{\bullet-}$. At pH 12, the highly alkaline conditions enabled the release of V ions from VO_2 into solution and inhibited the transfer process of e^- from Fe-VO_2 to PDS, resulting in a decrease in the degradation effect of MNZ.

The effects of different anions and cations on the photodegradation process of MNZ by the Fe-VO_2/PDS/Vis system were shown in Fig. 3e. The experimental results demonstrated that metal ions, such as K^+ and Ca^{2+}, and anions, such as NO_3^-, HPO_4^{2-}, SO_4^{2-}, and Cl^-, had less influence on the photodegradation process of MNZ. For HCO_3^-, the photodegradation process was mainly inhibited by increasing the solution pH and promoting the conversion of $SO_4^{\bullet-}$ to $^{\bullet}OH$. The HCO_3^-could regulate the pH of the system, but excess HCO_3^- would react with $SO_4^{\bullet-}$ as well as $^{\bullet}OH$ to form $^{\bullet}HCO_3$ [63], which the redox potential was lower than that of $SO_4^{\bullet-}$ and $^{\bullet}OH$, leading to a decrease in MNZ removal. In addition, the HCO_3^- would also react with Fe^{3+} in the solution, thus inhibiting the PDS activation process. After the addition of SCN^-, the photodegradation efficiency of MNZ reduced to 23%, which was attributed to the reaction of SCN^- with Fe^{3+} to form $Fe(SCN)_3$ [64], resulting in the loss of active sites for persulfate activation and increased complexation of photogenerated e^--h^+ pairs.

In order to verify the practicality of the Fe-VO_2/PDS/Vis system, actual water samples were collected in two different areas and MNZ degradation was investigated (Fig. 3g). The effects of different water qualities, such as underground water, surface water, tap water, distilled water and purified water, on the photodegradation ability of the Fe-VO_2/PDS/Vis system were investigated. As shown in Fig. 3f, the photodegradation rates of MNZ in underground water, surface water, tap water, distilled water and purified water were 34%, 98%, 63%, 94% and 97%, respectively. The Fe-VO_2/PDS/Vis system was confirmed to be resistant to environmental perturbations.

The reusability experiments of as-fabricated photocatalysts were presented in Text S3 (Supporting information.).

In VO_2 (Fig. 3h), the V lost electron upon the adsorption of PDS, indicating that V was a decomposition site that allowed PDS to react with V atoms. Meanwhile, the DFT calculations in Fig. 3i demonstrated that the Fe lost electron upon the adsorption of PDS on the Fe-VO_2 surface, suggesting that Fe exists as an active site on

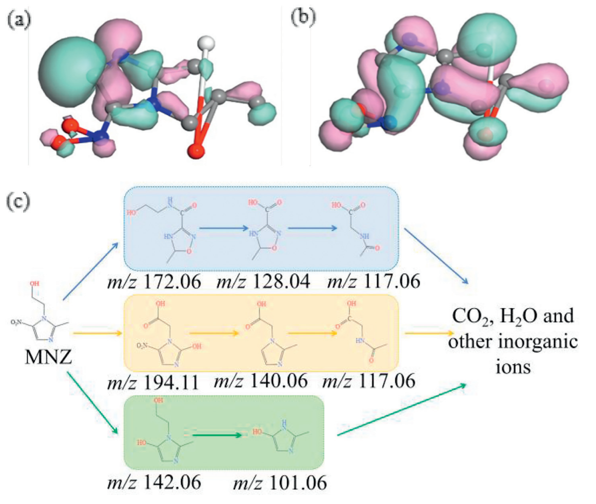

Fig. 4. (a) HOMO and (b) LUMO orbit images of MNZ. (c) The proposed pathways for MNZ photodegradation.

the surface of the material during the reaction. Moreover, a pattern of lost electrons can be found on nearby V atoms, also suggesting that V can transfer internal electrons within the material to provide enough electrons for the cyclic reaction on Fe. Thus, the system achieved rapid and stable catalytic system reaction of the material through the joint action of the two active sites for PDS activation.

In order to further investigate the degradation pathway of MNZ by Fe-VO_2/PDS/Vis system, MNZ intermediates were detected by HPLC-MS (Fig. S6 in Supporting information). Moreover, the frontier orbitals and Fuki Index of MNZ were computed by DFT to clarify the photodegradation pathway. The HOMO and LUMO orbits of MNZ were revealed by the light stability of their molecular structures (Figs. 4a and b), so it is difficult to self-degrade under natural conditions. The Fukui index describes radical attack (f^0) of the atoms on the MNZ molecule which was calculated by DFT (Table S3 in Supporting information). The atoms with larger f^0 were vulnerable to attack by reactive species, such as C (10), C (2), C (6), O (11), N (3), O (14), O (13), and C (1) marked in Table S3 (Supporting information). Therefore, the C–N bond and the imidazole ring can be broken easily by attack. Combined with computational outcomes, and the detected intermediates by HPLC-MS, three photodegradation pathways of MNZ was proposed (Fig. 4c). Pathway I, MNZ was converted to $m/z = 172.06$ after structural rearrangement, which was further converted to $m/z = 128.04$ by attacking the C–N bond by reactive radicals, and the imidazole ring-opened to form acetylglycine with $m/z = 117.06$ during the subsequent reaction. Pathway II, MNZ turned hydroxyl into carboxyl group generating $m/z = 194.11$ under the attack of h^+, replacing hydroxyl and nitro groups on imidazole ring to form $m/z = 140.06$ as by-products, while the $O_2^{\bullet -}$ can attack imidazole ring during degradation to make $m/z = 117.06$ as ionic fragments. Pathway III, MNZ denitrification generates $m/z = 142.06$, and the hydroxyethyl group was removed under the attack of reactive groups to form $m/z = 101.07$ [65,66]. MNZ molecules and intermediates may be oxidized to other small molecules and ultimately mineralized to H_2O and CO_2. These results agreed with the TOC analyses (Fig. S3 in Supporting information).

To confirm that the Fe-VO_2 activated sulfite to produce active free radicals, the selective reactive oxygen species (ROS) quenching tests and the ESR test were carried out. As shown in Fig. 5a, the furfuryl alcohol, *t*-BuOH, sodium oxalate, BQ and MeOH are used to capture $^1O_2$, $^{\bullet}OH$, h^+, $O_2^{\bullet -}$, and $SO_4^{\bullet -}$, respectively. After the addition of MeOH, the degradation of the MNZ was suppressed, and its degradation efficiency was reduced from 98% to 71%, indicating that $SO_4^{\bullet -}$ was one of the main active radicals. When sodium oxalate and BQ were added, the degradation of MNZ was inhibited, indicating that h^+ and $O_2^{\bullet -}$ were also the main active radicals. The degradation rate of the MNZ also declined when the Furfuryl alcohol and *t*-BuOH were added, suggesting that $^1O_2$ and $^{\bullet}OH$ also partially contribute to the degradation of MNZ. As shown in Figs. 5b and c, $SO_4^{\bullet -}$, $^{\bullet}OH$ and $^1O_2$ appeared in the Fe-VO_2 system, indicating the excellent oxidizing ability of Fe-VO_2/PDS under visible light. In addition, $O_2^{\bullet -}$ was detected under light conditions (Fig. 5d), suggesting that $O_2^{\bullet -}$ also played a role in the degradation of MNZ. The ESR results were in agreement with the selective ROS quenching tests.

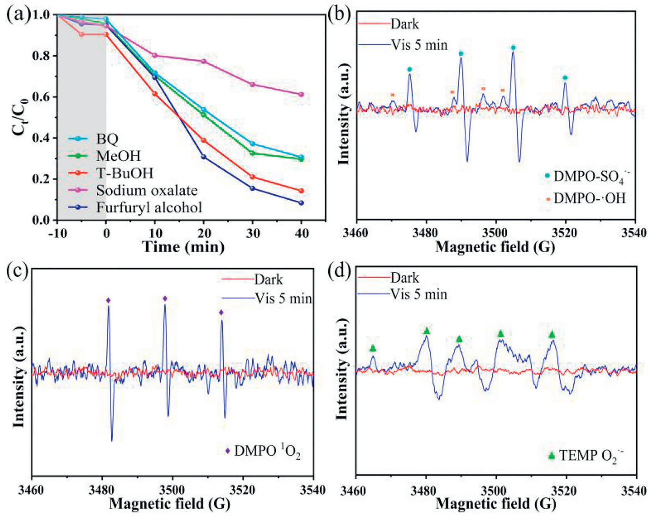

Fig. 5. (a) Free radical quenching experiment on photocatalytic degradation of MNZ. ESR spectra of Fe-VO_2 sample for (b) DMPO– $SO_4^{\bullet -}$ and $^{\bullet}OH$, (c) TMPO–$^1O_2$, and (d) DMPO–$O_2^{\bullet -}$.

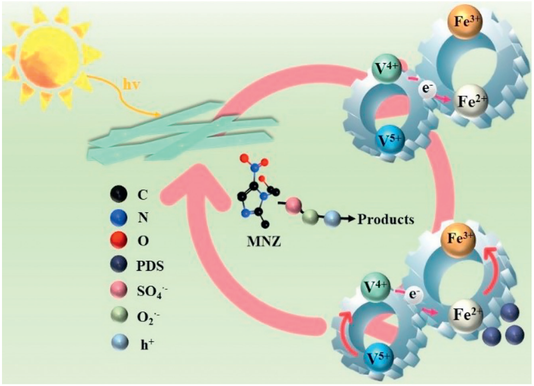

Fig. 6. Possible mechanism of Fe-VO_2/PDS/Vis degradation of MNZ.

Based on the above results, the possible degradation mechanism of the Fe-VO_2/PDS/Vis system was illustrated in Fig. 6, according to the Eqs. 1-12:

$$\text{Fe-VO}_2 + h\nu \rightarrow h^+\ (\text{Fe-VO}_2) + e^-\ (\text{Fe-VO}_2) \tag{1}$$

$$Fe^{3+} + e^- \rightarrow Fe^{2+} \tag{2}$$

$$Fe^{2+} + S_2O_8{}^{2-} \rightarrow Fe^{3+} + SO_4{}^{2-} + SO_4{}^{\bullet -} \tag{3}$$

$$h^+ + MNZ \rightarrow CO_2 + V^{4+} + H_2O \tag{4}$$

$$Fe^{3+} + S_2O_8{}^{2-} \rightarrow Fe^{2+} + S_2O_8{}^{\bullet -} \tag{5}$$

$$S_2O_8^{\bullet -} + O_2 \rightarrow S_2O_8^{2-} + O_2^{\bullet -} \tag{6}$$

$$SO_4^{\bullet -} + OH^- \ (H_2O) \rightarrow SO_4^{2-} + {}^{\bullet}OH \tag{7}$$

$$O_2 + e^- \rightarrow O_2^{\bullet -} \tag{8}$$

$$O_2^{\bullet -} + h^+ \rightarrow {}^1O_2 \tag{9}$$

$$O_2^{\bullet -} + O_2^{\bullet -} \rightarrow 2{}^1O_2 \tag{10}$$

$$O_2^{\bullet -} + {}^{\bullet}OH \rightarrow {}^1O_2 + OH^- \tag{11}$$

$$SO_4^{\bullet -},\ O_2^{\bullet -},\ h^+,\ {}^{\bullet}OH,\ {}^1O_2 + MNZ \rightarrow CO_2 + H_2O \tag{12}$$

VO_2 was excited by visible light to generate e^--h^+ pairs, in which the jump of e^- to the conduction band induced the conversion of Fe^{3+} to Fe^{2+}, and the Fe^{2+} in solution promoted the activation of PDS to produce $SO_4^{\bullet -}$, constructing an external cycle of Fe ions. And the electron-loss of V^{4+} was reconverted to V^{4+} through the oxidation of MNZ by V^{5+}, forming an inner cycle of V ions. When the conduction band potential of the semiconductor was lower than $O_2/O_2^{\bullet -}$ (−0.33 eV), then the reduction reaction converted the dissolved O_2 to $O_2^{\bullet -}$, and the conduction band potential of VO_2 was −0.23 eV, thus generating $O_2^{\bullet -}$ radicals. Additionally, PDS, which acts as an electron acceptor, can also formed $O_2^{\bullet -}$, ${}^1O_2$, and ${}^{\bullet}OH$ together through electron reactions contributing to the degradation process of MNZ.

In summary, an innovative strategy was developed to synthesize atomically dispersed Fe-doped VO_2 nanobelt catalysts by a simple hydrothermal calcination method, which effectively and stably removed MNZ. The significant electronegativity difference between Fe and V drove the electron transfer from V to Fe within the lattice. The dual cycling between Fe atoms and VO_2 nanobelts allowed the more efficient charge carriers separation and transfer in photocatalysis, and rapid activation of PDS to generate free radicals such as $SO_4^{\bullet -}$ for the removal of various antibiotics. This work provided new ideas for single atoms anchored into the oxide lattice for sustainable and efficient practical water remediation.

Declaration of competing interest

The authors declare that they have no known competing financial interests or personal relationships that could have appeared to influence the work reported in this paper.

CRediT authorship contribution statement

Shukun Le: Conceptualization, Investigation, Writing – original draft. **Peng Wang:** Data curation, Formal analysis. **Yuhao Liu:** Methodology. **Mutao Xu:** Project administration. **Quansheng Liu:** Resources, Validation. **Qijie Jin:** Investigation, Visualization. **Jie Miao:** Investigation. **Chengzhang Zhu:** Methodology, Resources, Supervision. **Haitao Xu:** Resources, Writing – review & editing.

Acknowledgments

The authors gratefully acknowledge the financial supports from the National Key Research and Development Program of China (Nos. 2021YFB3500600, 2021YFB3500605, 2022YFB3504100), Key R&D Program of Jiangsu Province (No. BE2022142), Ministry of Education Chunhui plan international cooperation project (No. 202200554), National Natural Science Foundation of China (No. grant 22208170), Natural Science Foundation of Inner Mongolia (No. 2021BS02016), Jiangsu International Cooperation Project (No. BZ2021018), Nanjing Science and Technology Top Experts Gathering Plan, and Open Foundation of State Environmental Protection Key Laboratory of Soil Environmental Management and Pollution Control (No. SEMPC2023004), Cooperation Foundation for the Chunhui Plan Program of Ministry of Education of China (No. 202200554), Open Project Program of Key Laboratory of Optic-electric Sensing and Analytical Chemistry for Life Science (No. M2024-7), MOE.

Supplementary materials

Supplementary material associated with this article can be found, in the online version, at doi:10.1016/j.cclet.2024.110087.

References

[1] H.J. Wang, J. Zhang, P. Wang, Chin. Chem. Lett. 31 (2020) 2789–2794.
[2] S.Y. Yu, Z.H Xie, X. Wu, et al., Chin. Chem. Lett. 35 (2024) 108714.
[3] X.D. Yang, J. Duan, X. Zhang, et al., Chin. Chem. Lett. 33 (2022) 3792–3796.
[4] P.M. Sathya, H. Mohan, J. Venkatachalam, K.K. Seralathan, Chemosphere 313 (2023) 137485.
[5] F. Chen, Y.H. Zhang, H.W. Huang, Chin. Chem. Lett. 34 (2023) 107523.
[6] Z.Q. Zhang, J.L. Liang, W. Zhang, et al., Appl. Catal. B: Environ. 330 (2023) 122621.
[7] C. Wang, H.Y. Liu, G.F. Wang, et al., J. Alloy. Compd. 917 (2022) 165507.
[8] Z.X. Yang, Z.Z. Wang, J.T. Wang, Y. Li, G.K. Zhang, Environ. Sci. Technol. 56 (2022) 18008–18017.
[9] M. Alsaidi, F.A. Azeez, L.A. Al-Hajji, A.A. Ismail, J. Environ. Manage. 314 (2022) 115047.
[10] C. Lykos, T. Kourkouta, I. Konstantinou, Sci. Total Environ. 870 (2023) 161877.
[11] L. Äystö, N. Vieno, P. Fjäder, J. Mehtonen, T. Nystén, Ecotox. Environ. Safe. 262 (2023) 115149.
[12] W.Y. Peng, Y. Fu, L.L. Wang, et al., Chin. Chem. Lett. 32 (2021) 2544–2550.
[13] K. Tian, L.M. Hu, L.M. Li, et al., Chin. Chem. Lett. 33 (2022) 4461–4477.
[14] S.K. Le, C.Z. Zhu, Y.W. Cao, et al., Appl. Catal. B: Environ. 303 (2022) 120903.
[15] Y. Lei, Y.F. Yu, X. Lei, et al., Environ. Sci. Technol. 57 (2023) 5433–5444.
[16] M.X. Ran, H. Xu, Y. Bao, et al., Angew. Chem. Int. Ed. 135 (2023) e202303728.
[17] A. López-Francés, F. Bernat-Quesada, M. Cabrero-Antonino, et al., Appl. Catal. B: Environ. 336 (2023) 122924.
[18] F. Ye, Y.M. Su, R.P. Li, et al., Appl. Catal. B: Environ. 337 (2023) 122992.
[19] H.Y. Zhu, M.T. Liu, G. Wang, et al., Rare Met. 43 (2024) 1686–1701.
[20] M.T. Liu, H.Y. Zhu, R.R. Du, et al., J. Environ. Chem. Eng. 11 (2023) 109939.
[21] S.Q. Yang, W.X. Zhang, M.T. Liu, et al., J. Environ. Chem. Eng. 11 (2023) 109190.
[22] R.R Du, H.Y. Zhu, H.Y. Zhao, et al., Environ. Res. 222 (2023) 115365.
[23] X. Li, S.W. Wang, P. Chen, et al., Appl. Catal. B: Environ. 325 (2023) 122401.
[24] G. Wang, K. Wang, Z.Y. Liu, et al., Appl. Catal. B: Environ. 325 (2023) 122359.
[25] Y.A. Li, J. Wei, N. Cui, et al., Adv. Funct. Mater. 33 (2023) 2301229.
[26] M.P. Zhu, J.C.E. Yang, D.Q. Guan, et al., Appl. Catal. B: Environ. 329 (2023) 122570.
[27] S.S. Li, M.H. Zhou, H.Z. Wu, et al., Appl. Catal. B: Environ. 338 (2023) 123064.
[28] B. Ko, J.Y. Chae, T. Badloe, et al., ACS Appl. Mater. Interfaces 14 (2022) 1404–1412.
[29] M.X. Bai, J.F. Gao, Z.H. He, J.F. Hou, L.B. Kong, J. Electroanal. Chem. 907 (2022) 116039.
[30] B.B. Shuai, C. Zhou, Y.Q. Pi, X. Xu, ACS Appl. Energ. Mater. 5 (2022) 6139–6145.
[31] Z.P. Zheng, Y. Luo, H. Yang, et al., Phys. Chem. Chem. Phys. 24 (2022) 8846–8853.
[32] R. Shi, Y.H. Wu, Z.Q. Xin, et al., Angew. Chem. Int. Ed. 62 (2023) e202301421.
[33] M. Jourshabani, M.R. Asrami, B.K. Lee, Small 19 (2023) 2300147.
[34] X.Y. Li, Z.C. Zhuang, J. Chai, et al., Nano Lett. 23 (2023) 2905–2914.
[35] F. Yang, X.Y. Chu, J.H. Sun, et al., Chin. Chem. Lett. 31 (2020) 2784–2788.
[36] D.C. Yang, Y.C. Xu, K. Pan, et al., Chin. Chem. Lett. 33 (2022) 378–384.
[37] J. Wang, B. Gao, D.L. Liu, et al., Nanomaterials 13 (2023) 443.
[38] Y. Chen, P.M. Wang, Z.T. Chen, B. Li, ACS Appl. Mater. Inter. 15 (2023) 46982–46994.
[39] C. Yang, S.S. Shang, Y. Fan, et al., Appl. Catal. B: Environ. 325 (2023) 122344.
[40] C.Z. Zhu, Q.Y. He, T.Y. Sun, et al., Chem. Eng. J. 464 (2023) 142704.
[41] J.Y. Qin, Y. Pei, Y. Zheng, D.Q. Ye, Y. Hu, Appl. Catal. B: Environ. 325 (2023) 122346.
[42] S.W. Du, S.Q. Lin, K.K. Ren, C.H. Li, F.X. Zhang, Appl. Catal. B: Environ. 328 (2023) 122503.
[43] W.Q. Li, S.Q. Xia, Z.Y. Wang, et al., Appl. Catal. B: Environ. 325 (2023) 122358.
[44] Y.X. Deng, M.Y. Xing, J.L. Zhang, Appl. Catal. B: Environ. 211 (2017) 157–166.
[45] Y. Ji, Z.L. Song, Y. Xu, Y.L. Zhang, J. Alloy. Compd. 925 (2022) 166655.
[46] J.S. Hu, P.F. Zhang, W.J. An, et al., Appl. Catal. B: Environ. 245 (2019) 130–142.
[47] C.V. Reddy, R.R. Kakarla, J. Shim, T.M. Aminabhavi, Chemosphere 308 (2022) 136414.
[48] A. Mancuso, N. Morante, M. De Carluccio, et al., Chem. Eng. J. 450 (2022) 138107.
[49] A. Zhou, C. Zhao, J.C. Zhou, et al., J. Mater. Chem. A 11 (2023) 12950–12957.
[50] C.H. Gao, J.J. Liu, M.L. Jia, G. Sa, A.J. Xu, Dye. Pigment. 212 (2023) 111115.

[51] D. Kuzyaka, C. Uzun, I. Yıldız, M. Kaya, B. Akata, Micropor. Mesopor. Mat. 323 (2021) 111256.
[52] X. Yang, J. Zou, J. Alloy. Compd. 940 (2023) 168868.
[53] W.L. Zhou, X.J. Li, X. Li, et al., Chem. Eng. J. 470 (2023) 144146.
[54] A. Shamloufard, S. Hajati, A.A. Youzbashi, et al., Appl. Surf. Sci. 590 (2022) 153118.
[55] B.L. Lin, Z.Y. Guo, J.H. Li, et al., Chem. Eng. J. 458 (2023) 141443.
[56] S. Ibraheem, G. Yasin, A. Kumar, et al., Appl. Catal. B: Environ. 304 (2022) 120987.
[57] A.K.S. Kumar, R.G. Compton, ACS Catal. 12 (2022) 4754–4764.
[58] D. Kuzyaka, C. Uzun, I. Yıldız, M. Kaya, B. Akata, Micropor. Mesopor. Mat. 323 (2021) 111256.
[59] B. Janani, M.K. Okla, S.S. Al-Amri, et al., Chemosphere 296 (2022) 134012.
[60] N. Kumar, S. Upadhyay, S. Chetana, et al., Mater. Lett. 335 (2023) 133810.
[61] H.C. Yan, C. Lai, S.Y. Liu, et al., Water Res. 234 (2023) 119808.
[62] P. Huang, P. Zhang, C.P. Wang, J.C. Tang, H.W. Sun, Appl. Catal. B: Environ. 303 (2022) 120926.
[63] M.D. Jiang, J.H. Lu, Y.F. Ji, D.Y. Kong, Water Res. 116 (2017) 324–331.
[64] Q.Y. Wu, Y. Zhang, H. Liu, et al., Water Res. 224 (2022) 119022.
[65] M.L. Tran, C.C. Fu, R.S. Juang, Environ. Sci. Pollut. Res. Int. 26 (2019) 11846–11855.
[66] M.L. Tran, C.C. Fu, R.S. Juang, Environ. Sci. Pollut. Res. Int. 25 (2018) 28285–28295.